



Organic phosphors with bright triplet excitons for efficient X-ray-excited luminescence

Xiao Wang^{1,10}, Huifang Shi^{2,10}, Huili Ma², Wenpeng Ye², Lulu Song², Jie Zan³, Xiaokang Yao², Xiangyu Ou³, Guohui Yang², Zhu Zhao², Manjeet Singh², Chongyang Lin², He Wang², Wenyong Jia², Qian Wang², Jiahuan Zhi², Chaomin Dong², Xueyan Jiang², Yongan Tang⁴, Xiaoji Xie⁵, Yang (Michael) Yang⁶, Jianpu Wang⁷, Qiushui Chen³, Yu Wang⁴, Huanghao Yang³, Guoqing Zhang⁶, Zhongfu An^{1,2}✉, Xiaogang Liu^{7,8}✉ and Wei Huang^{1,2,9}✉

Materials that exhibit X-ray-excited luminescence have great potential in radiation detection, security inspection, biomedical applications and X-ray astronomy^{1–5}. However, high-performance materials are almost exclusively limited to ceramic scintillators, which are typically prepared under high temperatures⁶. Herein we report metal-free organic phosphors based on a molecular design that supports efficient triplet exciton harvesting to enhance radioluminescence. These organic scintillators exhibit a detection limit of 33 nGy s^{–1}, which is 167 times lower than the standard dosage for X-ray medical examination and we demonstrate their potential application in X-ray radiography. These findings provide a fundamental design principle and new route for the creation of promising alternatives to incumbent inorganic scintillators. Furthermore, they offer new opportunities for development of flexible, stretchable X-ray detectors and imagers for non-destructive radiography testing and medical imaging.

X-ray-responsive materials that display large X-ray attenuation coefficients due to heavy element constituents have found important applications for bioimaging, radiotherapy and non-destructive testing^{7–11}. Conventional X-ray-responsive materials include non-emissive radiocontrast agents (for example, iohexol and iopromide) and ceramic scintillators that can convert high-energy X-ray beams into low-energy visible photons^{2,12,13}. So far, almost all reported X-ray scintillators are limited to inorganic phosphors or heavy-metal-containing organometallic complexes¹⁴. Metal-free organic phosphors have congenital advantages as scintillators, including abundant resource supplies, high mechanical flexibility, easy processing and large-area fabrication; however, weak X-ray absorption and inefficient exciton utilization have hindered development of organic-molecule-based scintillators¹³. Organic phosphors are mainly composed of light atoms such as carbon, hydrogen and nitrogen, resulting in weak X-ray absorption (attenuation coefficient $\mu \propto Z^4$, Supplementary Equation (1)). Besides, the weak spin–orbit coupling in conventional organic phosphors only generates

fluorescence from singlet excitons following irradiation. In principle, approximately 75% excitons are not well utilized, attributable to the dark state characteristic of the triplet excitons in metal-free organic phosphors^{15–17}.

Phosphorescence can be generated from bright triplet excitons in organic luminescent materials at room temperature^{18–29}. One strategy to realize room-temperature phosphorescence is to promote intersystem crossing (ISC) through heavy halogen atoms or aromatic carbonyl groups. Notably, the ISC rate constant (k_{ISC}) is proportional to the eighth power of the atomic number³⁰ ($k_{\text{ISC}} \propto Z^8$, Supplementary Equation 2), indicating that heavy atoms can efficiently populate triplet excitons. Another strategy is to suppress non-radiative energy dissipation by constructing a rigid environment through crystal engineering, host–guest doping or polymerization^{31–33}. As halogen atoms can efficiently harvest triplet excitons due to enhanced spin–orbit coupling, we therefore speculate that modulation of heavy halogen atoms may enhance radioluminescence of organic chromophores (Fig. 1a).

We designed and synthesized a series of halogen-atom-containing organic material systems to validate our hypothesis (Fig. 1b). Oxygen and nitrogen atoms were also incorporated in molecular frameworks for enhanced $n-\pi^*$ transitions, facilitating the ISC process³⁴. As a proof of concept, we first synthesized three isomers (*ortho*-ITC, *meta*-ITC and *para*-ITC) of 9,9'-(6-iodophenoxy-1,3,5-triazine-2,4-diyl)bis(9H-carbazole) with iodine atom modification at different positions. Their chemical structures and purities were characterized by ¹H- and ¹³C-NMR spectroscopies, single-crystal X-ray diffraction, elemental analysis and high-performance liquid chromatography (Supplementary Section 1 and Supplementary Fig. 1). Strong luminescence was detected under ultraviolet radiation (Fig. 2a insets and Supplementary Fig. 2) and persistent emission was observed by the naked eye for several seconds after removing the ultraviolet lamp (Fig. 2a insets). Moreover, we observed intense luminescence of these phosphors under X-ray excitation (Fig. 2b insets).

¹Frontiers Science Center for Flexible Electronics, Xi'an Institute of Flexible Electronics and Xi'an Institute of Biomedical Materials and Engineering, Northwestern Polytechnical University, Xi'an, China. ²Key Laboratory of Flexible Electronics and Institute of Advanced Materials, Nanjing Tech University, Nanjing, China. ³MOE Key Laboratory for Analytical Science of Food Safety and Biology, State Key Laboratory of Photocatalysis on Energy and Environment, College of Chemistry, Fuzhou University, Fuzhou, China. ⁴SZU–NUS Collaborative Innovation Center, ICL 2DMOST, Institute of Microscale Optoelectronics, Shenzhen University, Shenzhen, China. ⁵State Key Laboratory of Modern Optical Instrumentation, College of Optical Science and Engineering, International Research Center for Advanced Photonics, Zhejiang University, Hangzhou, Zhejiang, China. ⁶Hefei National Laboratory for Physical Sciences at the Microscale, University of Science and Technology of China, Hefei, China. ⁷Department of Chemistry, National University of Singapore, Singapore, Singapore. ⁸Institute of Materials Research and Engineering, A*STAR, Singapore, Singapore. ⁹Key Laboratory for Organic Electronics and Information Displays and Institute of Advanced Materials, Nanjing University of Posts and Telecommunications, Nanjing, China. ¹⁰These authors contributed equally: Xiao Wang, Huifang Shi. ✉e-mail: iamzf@njtech.edu.cn; chmlx@nus.edu.sg; iamwhuang@njtech.edu.cn

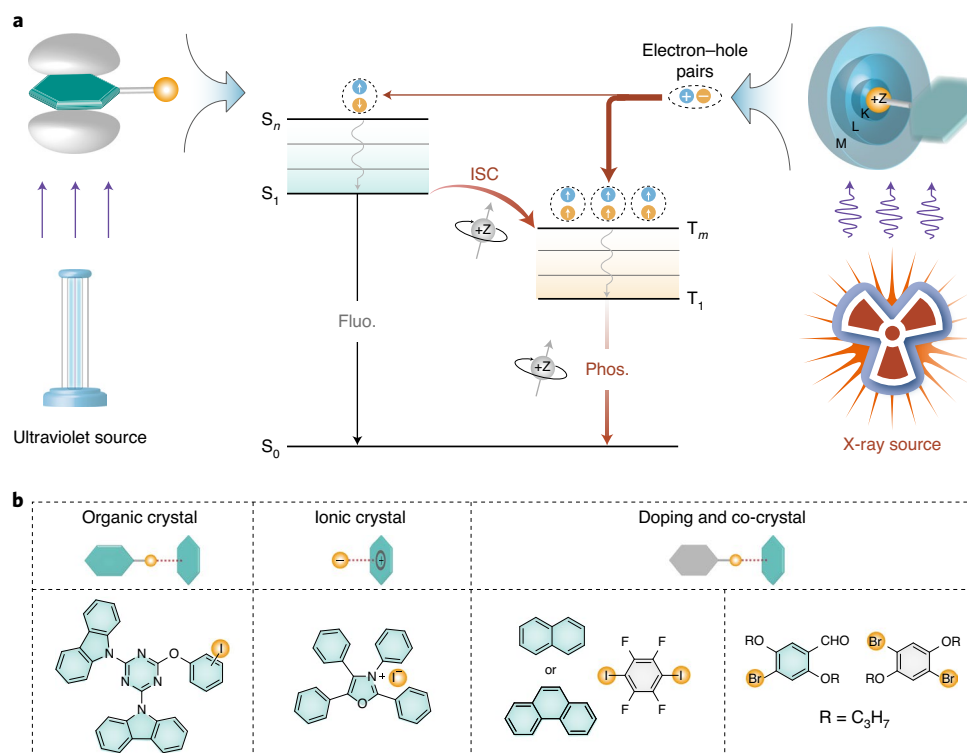


Fig. 1 | A schematic representation of the X-ray-excited luminescence in purely organic materials. **a**, A typical mechanism of ultraviolet-excited luminescence and the proposed X-ray-irradiated luminescence. Electrons at frontier molecular orbitals are excited by an ultraviolet source to generate singlet Frenkel excitons, representing the ultraviolet-light-absorption process. The molecules in excited states (S_n) then rapidly relax to the lowest vibrational level of S_1 , which then return to the ground state (S_0), accompanied by fluorescence (Fluo.). Molecules in the S_1 state can also undergo ISC to triplet states (T_m), which is followed by internal conversion to the lowest triplet state (T_1). However, the spin-forbidden origin of T_1 leads to a relatively weak phosphorescence (Phos.). For X-ray-excited luminescence, massive electrons and holes are first produced after the X-ray source excites the inner electrons of heavy atoms. The charge recombination then produces a larger ratio of triplet excitons according to spin statistics, populating triplet excitons to generate predominant phosphorescence. **b**, Rational design of purely organic molecules for X-ray-excited luminescence. Heavy atoms such as bromine and iodine are introduced to promote simultaneous X-ray absorption and ISC. Aromatic groups are designed to tune room-temperature phosphorescence properties. Types of phosphors are involved in the crystalline state, including organic crystals, ionic crystals, co-crystals and host-guest doping systems.

We then investigated the photoluminescence of the isomers in the solid state under ambient conditions. All three isomers showed dual emission bands with one at around 390 nm and the other in the 500–700 nm range (Fig. 2a). The latter emission band features long luminescence lifetimes of 46.5 ms for *o*-ITC (535 nm), 72.2 ms for *m*-ITC (525 nm) and 106 ms for *p*-ITC (530 nm) (Fig. 2c and Supplementary Table 1), indicating the phosphorescence nature of the emission. Vibrational emission peaks between 500 and 700 nm are separated by approximately $1,400\text{ cm}^{-1}$, signifying that the lowest excited triplet states are π -localized excited states. The maximum phosphorescence efficiencies of the *o*-ITC, *m*-ITC and *p*-ITC phosphors reach 38.2%, 37.1% and 19.1%, respectively (Supplementary Table 2).

In a further set of experiments, we explored radioluminescence behaviours of the isomers in the solid state. We found prominent bands of radioluminescence spectra at 535, 525, 530 nm for *o*-ITC, *m*-ITC and *p*-ITC, respectively (Fig. 2b). Compared with the photoluminescence spectra, the corresponding radioluminescence spectra displayed similar emission wavelengths but with notably enhanced phosphorescence (Fig. 2b). The phosphorescent nature of emission bands at lower energy was confirmed by decay measurements (Supplementary Fig. 3). It is worth mentioning that the integral area ratios of phosphorescence-to-fluorescence, derived from radioluminescence (13.59, 11.76 and 6.55 for *o*-ITC, *m*-ITC and *p*-ITC, respectively), are considerably larger than that from ultraviolet-excited counterparts (1.32, 0.81 and 0.48 for *o*-ITC,

m-ITC and *p*-ITC, respectively) (Fig. 2d). This finding indicates the existence of different photophysical mechanisms between photoluminescence and radioluminescence processes. The radioluminescence intensity of the *o*-ITC crystal was much higher than that of conventional organic scintillators (Supplementary Fig. 4), revealing the effect of heavy atom induction to molecular scintillators.

Given the efficient radioluminescence behaviour of *o*-ITC, we then selected it as a model to investigate its photostability. Importantly, when the phosphor was exposed to a high dose rate of X-ray ($278\text{ }\mu\text{Gys}^{-1}$) for a continuous 30 min, the radioluminescence intensity remained at around 94% of the initial value, which is comparable with that of commercial plastic scintillators (Supplementary Fig. 5). Moreover, the emission intensity of the organic phosphor was stable even under repeated X-ray excitation (130 on-off circles, Fig. 2e). Apart from photostability duration, the detection limit of X-ray dosage is also critical for practical applications. X-ray-excited luminescence intensities were linearly correlated with the dose rate of X-rays (Fig. 2f). The detection limit of 33 nGys^{-1} is approximately 167 times lower than the standard dosage for X-ray diagnostics ($5.5\text{ }\mu\text{Gys}^{-1}$; ref. ³⁵).

To gain a deep insight into the mechanism of X-ray-excited organic luminescence, we synthesized a series of *o*-ITC-based control molecules by substituting the iodine atom with bromine, chlorine or hydrogen. These control molecules are named *o*-BrTC, *o*-ClTC and *o*-HTC, respectively (Supplementary Scheme 1). We compared the absorption coefficients of the four molecules (*o*-ITC,

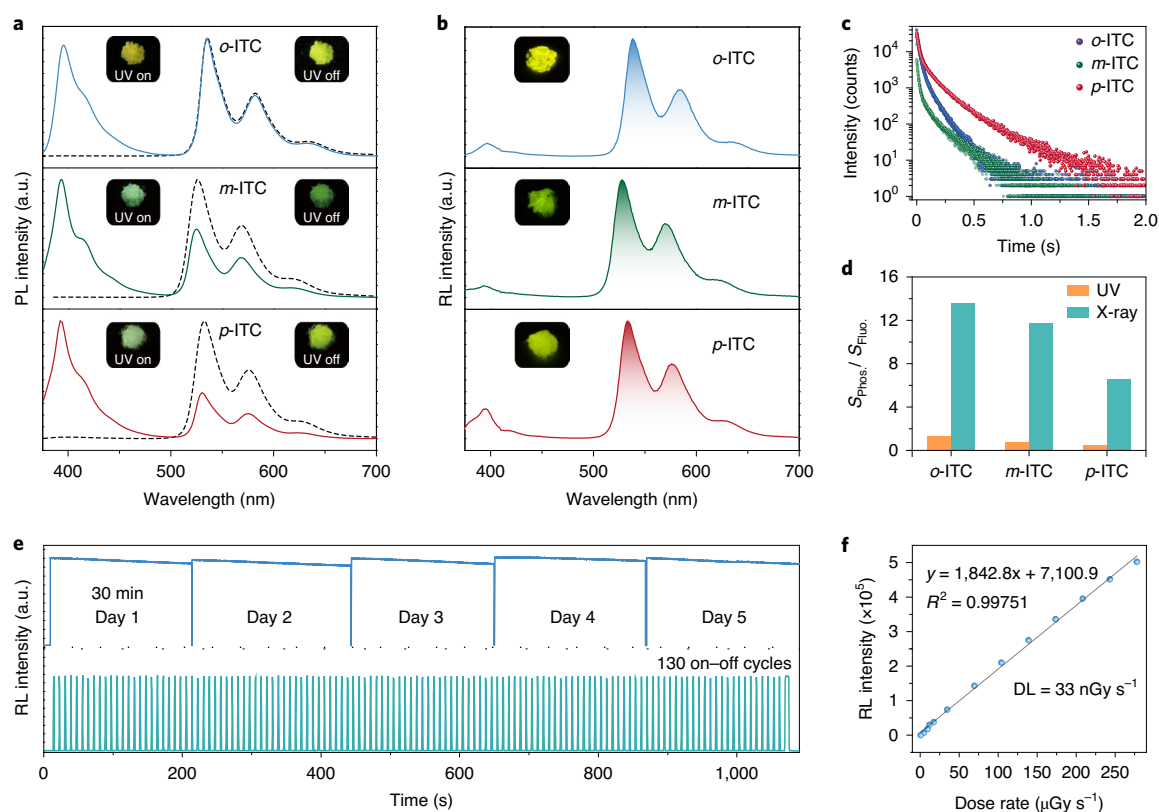


Fig. 2 | Photoluminescence and X-ray-excited luminescence characterization of iodine-containing isomers in the crystalline state under ambient conditions. **a**, Normalized steady-state photoluminescence (PL, solid lines) and room-temperature phosphorescence (dashed lines) spectra of *o*-ITC, *m*-ITC and *p*-ITC. The left insets are photographs of steady-state luminescence recorded under 365 nm excitation, whereas the right insets are photographs of phosphorescence after the ultraviolet source is removed. **b**, X-ray radioluminescence (RL) spectra of the three isomers at a dose rate of 278 $\mu\text{Gy s}^{-1}$. Insets are X-ray-excited photographs of the three isomers. **c**, The lifetime profiles of the ~ 530 nm emission bands of the isomers under excitation at 365 nm. **d**, The ratios of $S_{\text{Phos}}/S_{\text{Fluo}}$ under the excitation of ultraviolet and X-rays, where S_{Phos} and S_{Fluo} represent the integral area of the phosphorescence and fluorescence region, respectively. **e**, The emission photostability at 535 nm for the *o*-ITC phosphor versus continuous irradiation (top) and repeated on-off cycles of X-rays (bottom) at a dose rate of 278 $\mu\text{Gy s}^{-1}$. **f**, The dose rate dependence of the radioluminescence intensity of *o*-ITC in the range of 0.688 to 278 $\mu\text{Gy s}^{-1}$. The detection limit (DL) is calculated using the $3\sigma/\text{slope}$ method³⁷.

$Z_{\text{max}} = 53$, $K_{\alpha} = 33.2$ keV; *o*-BrTC, $Z_{\text{max}} = 35$, $K_{\alpha} = 13.5$ keV; *o*-ClTC, $Z_{\text{max}} = 17$, $K_{\alpha} = 2.82$ keV; *o*-HTC, $Z_{\text{max}} = 8$, $K_{\alpha} = 0.525$ keV) and confirmed the heavy atom effect in absorbing X-ray photons (Fig. 3a). Apart from resonant absorption edges, the absorption coefficient of *o*-ITC across the entire energy region (1–1,000 keV) is higher than that of *o*-BrTC, *o*-ClTC and *o*-HTC (Fig. 3a). This trend well matches the relative phosphorescence proportion in that there is a positive correlation between the phosphorescence proportion and the atomic number of heavy atoms (Fig. 3b). Furthermore, we conducted X-ray photoelectron spectroscopy to investigate escaped electrons from the surface of the *o*-ITC crystal (Supplementary Fig. 6). The generation of electrons and holes following X-ray irradiation was confirmed by photoconductive gain measurements (Fig. 3c; ref. 36).

Single-crystal analysis of *o*-ITC showed that each molecule is confined by neighbouring molecules with multiple intermolecular interactions, with distances of 2.615 (C–H \cdots O), 2.886 (C–H \cdots π), 3.303 ($\pi\cdots\pi$) and 3.481 Å (C–I $\cdots\pi$) (Fig. 3d and Supplementary Fig. 7). This confinement results in a rigid molecule structure that effectively suppresses non-radiative decay of triplet excitons. The short distance (3.428 Å) between the iodine atom and the carbazole plane enhances ISC between singlet and triplet states and ultimately efficient room-temperature phosphorescence. We performed first-principles, time-dependent density functional theory calculations to probe this mechanism (Supplementary Fig. 8). Spin-orbit

coupling constants (ξ) of S_1 to T_n for *o*-ITC (S_1 – T_2 , 2.79 cm^{-1}) were considerably larger than that of *o*-HTC without heavy atom constituents (S_1 – T_3 , 0.69 cm^{-1}). Furthermore, the rate constants for ISC (k_{ISC}) and phosphorescence (k_p) of the organic molecules increased following halogenation (Supplementary Table 3). For example, k_p of *o*-ITC is 11.6 s^{-1} , 120 times higher than that of *o*-HTC (0.097 s^{-1}). These results are consistent with heavy-atom-mediated ISC, supporting the feasibility of harvesting triplet excitons to improve radioluminescence.

All things considered together, we proposed a plausible mechanism that controls radioluminescence in metal-free organic scintillators (Fig. 3e). Three stages are probably involved during X-ray-excited luminescence. At the first stage, X-ray photons are mainly absorbed by heavy atoms of the molecule via the photoelectric effect. High-energy X-ray photons (5–50 keV) eject electrons from the inner shells of the atoms. Fast photoelectrons subsequently induce a large number of secondary electrons. Those high-energy electrons and holes are rapidly thermalized in the lowest unoccupied molecular orbital (LUMO) and the highest occupied molecular orbital (HOMO) of the organic molecules, respectively. The electrons and holes recombine to produce singlet and triplet excitons at a 1:3 ratio, according to spin statistics. The radiative decay processes of singlet and triplet excitons generate fluorescence and phosphorescence, respectively. Notably, the bright triplet excitons—due to strong spin–orbit coupling—render metal-free

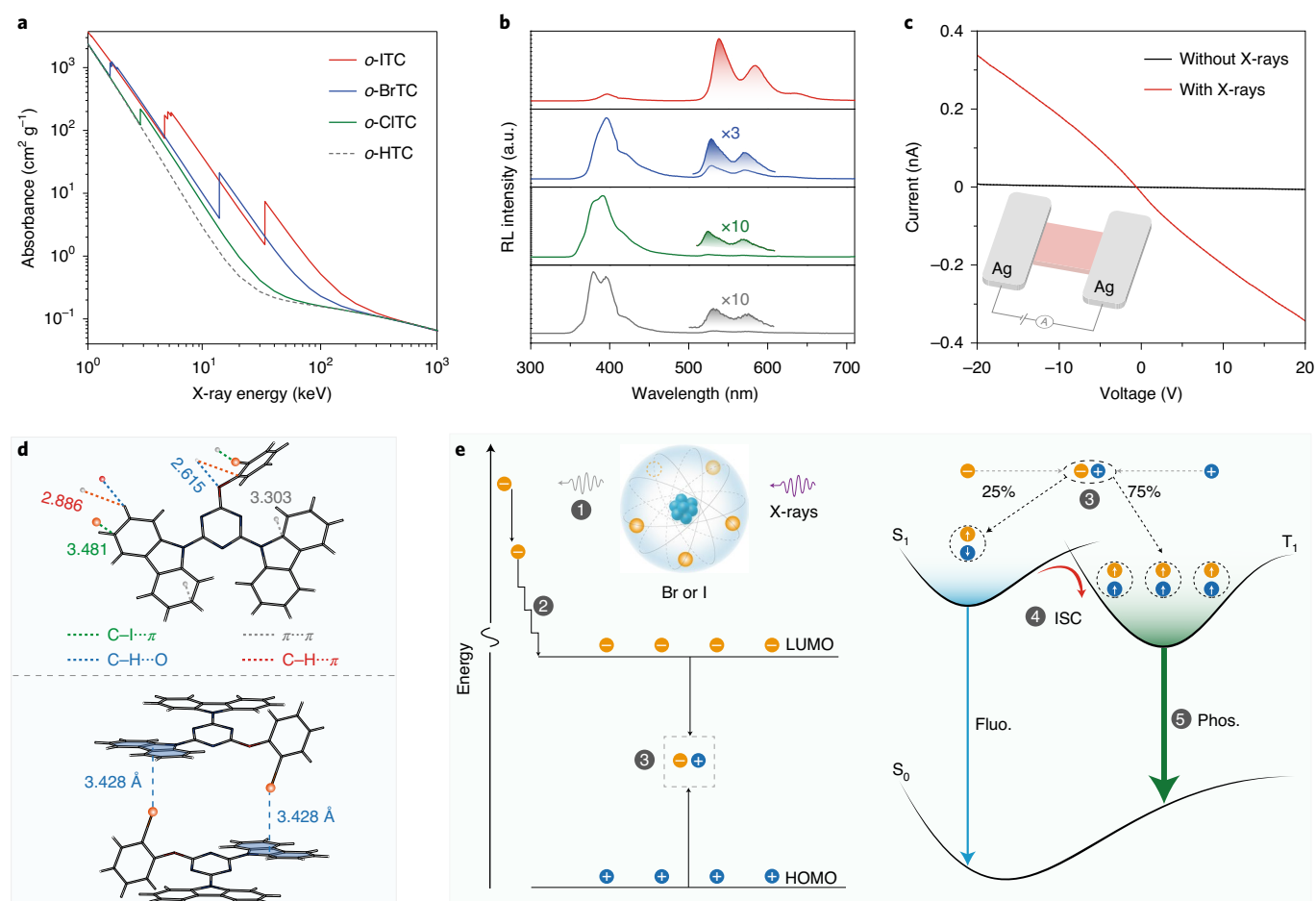


Fig. 3 | Proposed mechanism of X-ray-excited luminescence in purely organic molecules at room temperature. **a**, X-ray absorption spectra of *o*-ITC (red line), *o*-BrTC (blue line), *o*-CITC (green line) and *o*-HTC (dashed line) measured as a function of X-ray energy. The attenuation coefficient μ was obtained from the photon cross-section database³⁸. **b**, Radioluminescence spectra of *o*-ITC (red), *o*-BrTC (blue), *o*-CITC (green) and *o*-HTC (grey) phosphors at a dose rate of $278 \mu\text{Gy s}^{-1}$. The phosphorescent bands are multiplied by suitable times. **c**, Current-voltage curves of the constructed photodetector, measured in the dark and under X-ray illumination (dose rate = 2.094 mGy s^{-1}). The inset is a schematic construction of the photodetector. The silver electrodes are deposited onto the *o*-ITC crystal for hole-electron extraction; the distance between the two silver electrodes is 3 mm. **d**, The molecular arrangement of *o*-ITC molecules in a single crystal. Note that four types of intermolecular interactions between neighbouring molecules are shown in different colours. **e**, Plausible energy transfer processes for radioluminescence in organic molecules. Following X-ray excitation, electrons (orange circles) are ejected mainly from the inner shell of heavy atoms, generating high-energy holes (blue circles) in core levels (step 1). High-energy electrons then interact with outer shells of the atoms, resulting in an avalanche of secondary carriers. This process continues until the generated electrons and holes cease ionization, leading to thermalization in LUMO and HOMO (step 2). The recombination of electrons and holes produces excitons in a ratio of 25% singlet excitons to 75% triplet excitons (step 3). Intersystem crossing is enhanced due to the strong spin-orbit coupling (step 4), generating a dominant phosphorescent emission compared with ultraviolet-excited photoluminescence (step 5).

organic molecules with efficient phosphorescent radioluminescence compared with photoluminescence under ultraviolet excitation. The maximum proportion of singlet excitons from *o*-ITC was calculated as 22% under X-ray irradiation (Supplementary Section 2), which agrees with the theoretical value. We further compared the luminescent properties of *o*-BrTC, *o*-CITC and *o*-HTC molecules under ultraviolet or X-ray excitation. X-ray excitation spectra indeed displayed a larger proportion of phosphorescence (Supplementary Figs. 9 and 10).

We further synthesized various heavy-atom-containing materials, such as an organic ionic crystal (TPOI), co-crystals (NIFB and PIFB) and a doped crystal (C3BrA), to verify the generality of our main findings (Fig. 4a and Supplementary Scheme 1). All of these organic materials showed intense X-ray-excited luminescence with distinct emission colours. Specifically, TPOI showed radioluminescence at 586 nm, whereas NIFB and PIFB displayed radioluminescence with maximum emission peaks at 513 and 568 nm,

respectively. For the doped C3BrA crystal, the radioluminescence peak was centred at 516 nm. These materials display tunable visible emissions and lifetimes that span many orders of magnitude (Fig. 4b,c and Supplementary Fig. 11).

Regarding the intense X-ray-excited luminescence, we next applied *o*-ITC molecules to X-ray radiography. We first fabricated a flexible polydimethylsiloxane film of *o*-ITC as the background substrate (Supplementary Fig. 12), which showed the same radioluminescence as the bulk crystal. A crab specimen was then placed between the X-ray source and the *o*-ITC film (Fig. 4d). The hard shell of the crab could be directly visualized using a commercial digital camera (Fig. 4e). The application of this principle of X-ray contrast imaging also enabled inspection of the inner structures of an opaque capsule with a built-in metallic spring and a cylinder (Fig. 4f). These results demonstrate the potential of using organic molecules as flexible X-ray detectors for radiography applications. Furthermore, the flexible nature of the resulting

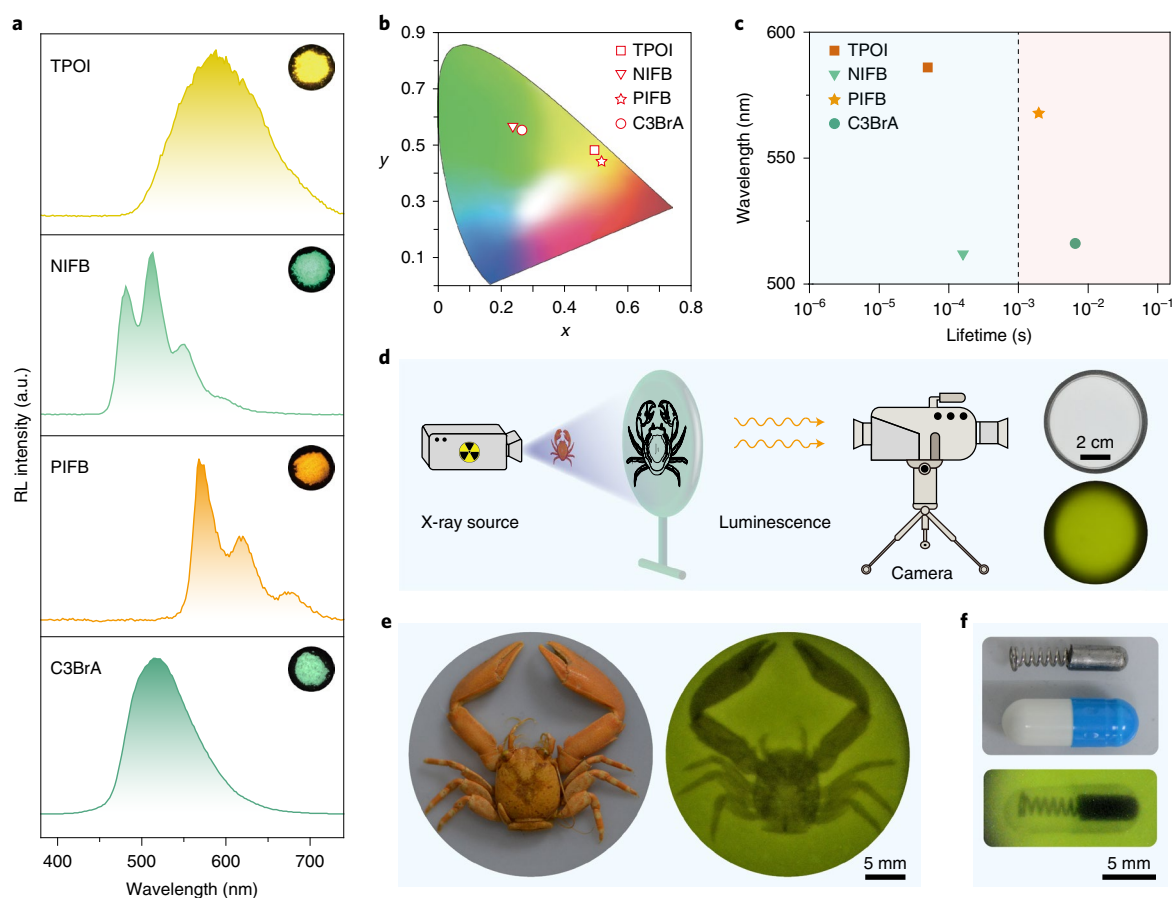


Fig. 4 | Versatile purely organic molecules for X-ray-excited luminescence and primary demonstration for radiography under ambient conditions.

a, Radioluminescence spectra and radioluminescent photographs (insets) of an ionic crystal (TPOI), co-crystals (NIFB and PIFB) and a doped system (C3BrA), recorded at a dose rate of $278 \mu\text{Gy s}^{-1}$. **b**, A CIE chromaticity coordinate diagram of the radioluminescence of the organic molecules. **c**, A plot of maximum emission wavelengths versus the average lifetimes of the organic molecules; the lifetimes range from microseconds to subseconds. **d**, A schematic of the radiography set-up. A polydimethylsiloxane film (diameter = 6 cm) containing o-ITC was used as the luminescent background and a crab specimen was placed between the X-ray source and a digital camera. **e**, Bright- (left) and dark-field (right) photographs of the specimen, recorded before and after X-ray exposure. **f**, Bright- (top) and dark-field (bottom) photographs of a capsule containing a metallic spring and a cylinder, recorded before and after X-ray exposure.

materials can be optimized to combine with 3D printing or inkjet-printing techniques for fabrication of X-ray detectors with various shapes.

In conclusion, we have reported a molecular design principle of metal-free organic molecules to achieve high-efficiency radioluminescence. The modulation of heavy halogen atoms in a series of designed organic molecules promotes X-ray absorption and ISC, leading to intense X-ray-excited luminescence under ambient conditions. Our approach is applicable to small molecular crystals, ionic crystals and host-guest systems, offering diverse emission colours and tunable radioluminescence lifetimes. The halogen atom effect can be harnessed to develop organic scintillators for non-destructive radiographic imaging at low levels of radiation exposure. Importantly, our finding not only provides a general design principle for achieving efficient X-ray-excited luminescence with organic molecules, but also will broaden the utility of organic phosphorescent materials for optoelectronic and bioimaging applications.

Online content

Any methods, additional references, Nature Research reporting summaries, source data, extended data, supplementary information, acknowledgements, peer review information; details of

author contributions and competing interests; and statements of data and code availability are available at <https://doi.org/10.1038/s41566-020-00744-0>.

Received: 12 August 2020; Accepted: 18 November 2020;
Published online: 11 January 2021

References

- Büchle, P. et al. X-ray imaging with scintillator-sensitized hybrid organic photodetectors. *Nat. Photon.* **9**, 843–848 (2015).
- Chen, Q. et al. All-inorganic perovskite nanocrystal scintillators. *Nature* **561**, 88–93 (2018).
- Yang, Y. et al. X-ray-activated long persistent phosphors featuring strong UVC afterglow emissions. *Light Sci. Appl.* **7**, 88 (2018).
- Fan, W. et al. Breaking the depth dependence by nanotechnology-enhanced X-ray-excited deep cancer theranostics. *Adv. Mater.* **31**, 1806381 (2019).
- Gandini, M. et al. Efficient, fast and reabsorption-free perovskite nanocrystal-based sensitized plastic scintillators. *Nat. Nanotechnol.* **15**, 462–468 (2020).
- Weber, M. J. Inorganic scintillators: today and tomorrow. *J. Lumin.* **100**, 35–45 (2002).
- Kim, Y. C. et al. Printable organometallic perovskite enables large-area, low-dose X-ray imaging. *Nature* **550**, 87–91 (2017).
- Shrestha, S. et al. High-performance direct conversion X-ray detectors based on sintered hybrid lead triiodide perovskite wafers. *Nat. Photon.* **11**, 436–440 (2017).

9. Pan, W. et al. Cs₂AgBiBr₆ single-crystal X-ray detectors with a low detection limit. *Nat. Photon.* **11**, 726–732 (2017).
10. Lu, K. et al. Low-dose X-ray radiotherapy–radiodynamic therapy via nanoscale metal–organic frameworks enhances checkpoint blockade immunotherapy. *Nat. Biomed. Eng.* **2**, 600–610 (2018).
11. Nikl, M. & Yoshikawa, A. Recent R&D trends in inorganic single-crystal scintillator materials for radiation detection. *Adv. Optical Mater.* **3**, 463–481 (2015).
12. Lusic, H. & Grinstaff, M. W. X-ray-computed tomography contrast agents. *Chem. Rev.* **113**, 1641–1666 (2012).
13. Hajagos, T., Liu, C., Cherepy, N. & Pei, Q. High-Z sensitized plastic scintillators: a review. *Adv. Mater.* **30**, 1706956 (2018).
14. Chen, X., Song, J., Chen, X. & Yang, H. X-ray-activated nanosystems for theranostic applications. *Chem. Soc. Rev.* **48**, 3073–3101 (2019).
15. Baldo, M. A., Thompson, M. E. & Forrest, S. R. High-efficiency fluorescent organic light-emitting devices using a phosphorescent sensitizer. *Nature* **403**, 750–753 (2000).
16. Rao, A. et al. The role of spin in the kinetic control of recombination in organic photovoltaics. *Nature* **500**, 435–439 (2013).
17. Thompson, N. J. et al. Energy harvesting of non-emissive triplet excitons in tetracene by emissive PbS nanocrystals. *Nat. Mater.* **13**, 1039–1043 (2014).
18. Zhang, G., Palmer, G., Dewhirst, M. & Fraser, C. A dual-emissive-materials design concept enables tumour hypoxia imaging. *Nat. Mater.* **8**, 747–751 (2009).
19. Yuan, W. et al. Crystallization-induced phosphorescence of pure organic luminogens at room temperature. *J. Phys. Chem. C* **114**, 6090–6099 (2010).
20. An, Z. et al. Stabilizing triplet excited states for ultralong organic phosphorescence. *Nat. Mater.* **14**, 685–690 (2015).
21. Yang, Z. et al. Intermolecular electronic coupling of organic units for efficient persistent room-temperature phosphorescence. *Angew. Chem. Int. Ed.* **55**, 2181–2185 (2016).
22. Lucenti, E. et al. Cyclic triimidazole derivatives: intriguing examples of multiple emissions and ultralong phosphorescence at room temperature. *Angew. Chem. Int. Ed.* **56**, 16302–16307 (2017).
23. Xie, Y. et al. How the molecular packing affects the room temperature phosphorescence in pure organic compounds: ingenious molecular design, detailed crystal analysis, and rational theoretical calculations. *Adv. Mater.* **29**, 1606829 (2017).
24. Wang, J. et al. A facile strategy for realizing room temperature phosphorescence and single molecule white light emission. *Nat. Commun.* **9**, 2963 (2018).
25. Su, Y. et al. Ultralong room temperature phosphorescence from amorphous organic materials toward confidential information encryption and decryption. *Sci. Adv.* **4**, 9732–9744 (2018).
26. Salla, C. A. et al. Persistent solid-state phosphorescence and delayed fluorescence at room temperature by a twisted hydrocarbon. *Angew. Chem. Int. Ed.* **58**, 6982–6986 (2019).
27. Ma, H., Peng, Q., An, Z., Huang, W. & Shuai, Z. Efficient and long-lived room-temperature organic phosphorescence: theoretical descriptors for molecular designs. *J. Am. Chem. Soc.* **141**, 1010–1015 (2019).
28. Wang, W., Zhang, Y. & Jin, W. Halogen bonding in room-temperature phosphorescent materials. *Coord. Chem. Rev.* **404**, 213107 (2020).
29. Li, W. et al. Selective expression of chromophores in a single molecule: soft organic crystals exhibiting full-colour tunability and dynamic triplet–exciton behaviours. *Angew. Chem. Int. Ed.* **59**, 3739–3745 (2020).
30. Baryshnikov, G., Minaev, B. & Ågren, H. Theory and calculation of the phosphorescence phenomenon. *Chem. Rev.* **117**, 6500–6537 (2017).
31. Bolton, O., Lee, K., Kim, H., Lin, K. & Kim, J. Activating efficient phosphorescence from purely organic materials by crystal design. *Nat. Chem.* **3**, 205–210 (2011).
32. Gu, L. et al. Colour-tunable ultra-long organic phosphorescence of a single-component molecular crystal. *Nat. Photon.* **13**, 406–411 (2019).
33. Zhang, T. et al. Molecular engineering for metal-free amorphous materials with room-temperature phosphorescence. *Angew. Chem. Int. Ed.* **59**, 11206–11216 (2020).
34. El-Sayed, M. A. Triplet state: its radiative and nonradiative properties. *Acc. Chem. Res.* **1**, 8–16 (1968).
35. Wei, H. et al. Sensitive X-ray detectors made of methylammonium lead tribromide perovskite single crystals. *Nat. Photon.* **10**, 333–339 (2016).
36. Zhuang, R. et al. Highly sensitive X-ray detector made of layered perovskite-like (NH₄)₂BiI₆ single crystal with anisotropic response. *Nat. Photon.* **13**, 602–608 (2019).
37. Long, G. & Winefordner, J. Limit of detection: a closer look at the IUPAC definition. *Anal. Chem.* **55**, 712A–724A (1983).
38. Berger, M. J. et al. *XCOM: Photon Cross Sections Database* (National Institute of Standards and Technology, 2013); <https://www.nist.gov/pml/xcom-photon-cross-sections-database>

Publisher's note Springer Nature remains neutral with regard to jurisdictional claims in published maps and institutional affiliations.

© The Author(s), under exclusive licence to Springer Nature Limited 2021

Data availability

The data that support the plots within this paper and other findings of this study are available from the corresponding author on reasonable request. Source data are provided with this paper.

Acknowledgements

This work is supported by the National Key R&D Program of China (grant no. 2020YFA0709900), the National Natural Science Foundation of China (grant nos. 21975120, 21875104, 91833304, 21973043, 51673095 and 61935017), the Joint Research Funds of Department of Science and Technology of Shaanxi Province and Northwestern Polytechnical University (grant no. 2020GXLH-Z-006), Natural Science Fund for Distinguished Young Scholars of Jiangsu Province (grant no. BK20180037), China National Postdoctoral Program for Innovative Talents (grant no. BX20200278), Projects of International Cooperation and Exchanges NSFC (grant no. 51811530018), the Fundamental Research Funds for the Central Universities, Agency for Science, Technology and Research (A*STAR) under its AME program (grant nos. A1883c0011 and A1983c0038), and the King Abdullah University of Science and Technology (KAUST) Office of Sponsored Research (OSR) under award no. OSR-2018-CRG7-3736.

Author contributions

X.W., H.S., Z.A., X.L. and W.H. conceived the experiments. X.W., H.S., Z.A., X.L. and W.H. prepared the paper. X.W., H.S., W.Y., L.S., X.Y., G.Y., Z.Z., M.S., C.L., J.Z.

and C.D. were primarily responsible for the experiments. J.Z., X.O., Y.T., Q.C., Y.W. and H.Y. were responsible for the X-ray related experiments. H.W., Q.W. and W.J. performed lifetime and quantum yield measurements. H.M. and X.J. contributed to time-dependent density functional theory calculations. Y(M).Y. conducted photoconductive gain measurements. X.X., J.W., Q.C. and G.Z. gave suggestions of conceptual ideas and language improvements for the manuscript. All authors contributed to the data analyses.

Competing interests

The authors declare no competing interests.

Additional information

Supplementary information is available for this paper at <https://doi.org/10.1038/s41566-020-00744-0>.

Correspondence and requests for materials should be addressed to Z.A., X.L. or W.H.

Peer review information *Nature Photonics* thanks the anonymous reviewers for their contribution to the peer review of this work.

Reprints and permissions information is available at www.nature.com/reprints.